

A Novel Thermal Model for the Lattice Boltzmann Method in Incompressible Limit

Xiaoyi He, Shiyi Chen, and Gary D. Doolen

*Theoretical Division and the Center for Nonlinear Studies, Los Alamos National Laboratory,
Los Alamos, New Mexico 87545*

Received December 16, 1997; revised June 25, 1998

A novel lattice Boltzmann thermal model is proposed for studying thermo-hydrodynamics in incompressible limit. The new model introduces an internal energy density distribution function to simulate the temperature field. The macroscopic density and velocity fields are still simulated using the density distribution function. Compared with the multispeed thermal lattice Boltzmann models, the current scheme is numerically more stable. In addition, the new model can incorporate viscous heat dissipation and compression work done by the pressure, in contrast to the passive-scalar-based thermal lattice Boltzmann models. Numerical simulations of Couette flow with a temperature gradient and Rayleigh–Bénard convection agree well with analytical solutions and benchmark data. © 1998 Academic Press

I. INTRODUCTION

The lattice Boltzmann equation (LBE) method as a relatively new numerical scheme has recently achieved considerable success in simulating fluid flows and associated transport phenomena [1]. Based on kinetic theory, the lattice Boltzmann method simulates fluid flows by tracking the evolution of the single-particle distribution. In simulations of the single-component, isothermal fluid flow, the lattice Boltzmann method was found to be as stable, accurate, and computationally efficient as classical computational methods [2–5]. In addition, this method has been shown to be particularly useful in applications involving interfacial dynamics and complex boundaries. Because the LBE method is intrinsically a mesoscopic approach based on simulating the evolution of the single particle distribution, the interparticle interaction can be naturally incorporated [6–9] and boundary conditions with complex geometries such as those in porous media can be easily implemented (see, e.g., [10]).

Although promising, the current lattice Boltzmann method still has a few shortcomings that limit its general application as a practical computational fluid dynamics tool. One of

these shortcomings, which is specifically addressed in this paper, is the lack of a satisfactory thermal model for heat transfer problems. In general, the previous thermal lattice Boltzmann models fall into two categories: the multispeed approach and the passive-scalar approach. The multispeed approach is a straightforward extension of the LBE isothermal models in which only the density distribution function is used [11–13]. To obtain the temperature evolution equation at the macroscopic level, additional speeds are necessary and the equilibrium distribution must include the higher-order velocity terms. Although this approach has been shown to be theoretically possible [11], previous models suffer severe numerical instability and the temperature variation is limited to a narrow range [14]. Some recent work may provide new directions for this type of approach [15,16].

The passive-scalar approach utilizes the fact that the macroscopic temperature satisfies the same evolution equation as a passive scalar if the viscous heat dissipation and compression work done by the pressure are negligible [17,18]. In a passive-scalar-based LBE thermal model, the temperature is simulated using a separate distribution function which is independent of the density distribution. The main advantage of the passive-scalar LBE thermal model over its multispeed counterpart is the enhancement of the numerical stability [17,18]. In addition, the accuracy of the passive-scalar model has been verified by several benchmark studies [18,19]. Obviously, this approach will become more useful if the viscous heat dissipation and compression work done by the pressure can be correctly incorporated into the model.

In this paper, we propose a novel thermal model for the lattice Boltzmann method which greatly improves the previous LBE thermal models. This new scheme is based on the recent discovery [20,21] that the LBE isothermal models can be directly derived by properly discretizing the continuous Boltzmann equation in temporal, spatial, and velocity spaces. Following the same procedure, an LBE thermal model can be derived by discretizing the continuous evolution equation for the internal energy distribution. The new scheme is similar to the passive-scalar approach because it also uses an independent distribution function to simulate the temperature evolution. Its numerical stability is similar to that of the passive-scalar LBE thermal models. On the other hand, because the new scheme directly simulates the evolution of the internal energy, the viscous heat dissipation and compression work done by the pressure can be naturally incorporated.

The rest of the paper is organized as follows. In Section II, the new distribution function of the internal energy is introduced and its evolution equation in the continuous regime is derived from the Boltzmann equation. This evolution equation is then proved to recover the desired macroscopic energy equation using the Chapman–Enskog expansion. In Section III, a new lattice Boltzmann thermal model is derived by discretizing the continuous evolution equation for the distribution function of the internal energy. Section IV presents numerical simulations of two classical heat transfer problems, Couette flow with a temperature gradient and Rayleigh–Bénard convection. The results are compared with theoretical solutions and other computational results. A brief conclusion is given in Section V.

II. INTERNAL ENERGY DISTRIBUTION AND ITS EVOLUTION FUNCTION

Kinetic theory states that the evolution of the single-particle density distribution in a fluid system obeys the Boltzmann equation

$$\partial_t f + (\boldsymbol{\xi} \cdot \nabla) f = \Omega(f), \quad (1)$$

where f is the single-particle density distribution function, $\boldsymbol{\xi}$ is the microscopic velocity, and Ω is the collision term. Macroscopic variables, such as the density ρ , velocity \mathbf{u} , and temperature T , can be calculated as the moments of the density distribution function:

$$\rho = \int f d\boldsymbol{\xi}, \quad (2)$$

$$\rho \mathbf{u} = \int \boldsymbol{\xi} f d\boldsymbol{\xi}, \quad (3)$$

$$\frac{\rho DRT}{2} = \int \frac{(\boldsymbol{\xi} - \mathbf{u})^2}{2} f d\boldsymbol{\xi}. \quad (4)$$

The collision term in the Boltzmann equation is very complicated and must be simplified in practical calculations. One such simplification is to replace the collision term by a single-relaxation-time BGK model [22]:

$$\partial_t \tilde{f} + (\boldsymbol{\xi} \cdot \nabla) \tilde{f} = -\frac{\tilde{f} - f^{eq}}{\tau_v}. \quad (5)$$

Here τ_v is the relaxation time and f^{eq} is the Maxwell–Boltzmann equilibrium distribution

$$f^{eq} = \frac{\rho}{(2\pi RT)^{D/2}} \exp\left[-\frac{(\boldsymbol{\xi} - \mathbf{u})^2}{2RT}\right], \quad (6)$$

where R is the gas constant and D is the dimension.

It is well known that, using the Chapman–Enskog expansion, the Boltzmann–BGK equation, Eq.(5), recovers the correct continuity and momentum equations at the Navier–Stokes level [23],

$$\partial_t \rho + \nabla \cdot (\rho \mathbf{u}) = 0, \quad (7)$$

$$\rho[\partial_t \mathbf{u} + (\mathbf{u} \cdot \nabla) \mathbf{u}] = -\nabla p + \nabla \cdot \boldsymbol{\Pi}, \quad (8)$$

where $p = \rho RT$ is the pressure and $\boldsymbol{\Pi}$ is the stress tensor,

$$\boldsymbol{\Pi} = \rho \nu (\nabla \mathbf{u} + \mathbf{u} \nabla), \quad (9)$$

where the kinetic viscosity ν is related to the relaxation time by $\nu = \tau_v RT$.

However, the Boltzmann equation with the single-relaxation-time BGK model does have one unsatisfactory feature: the energy equation obtained from the second moment of \tilde{f} yields a fixed Prandtl number, implying that the thermal conductivity cannot be adjusted independent of the kinetic viscosity [23]. Since we are interested in deriving a numerical scheme for general fluids with arbitrary Prandtl numbers, we choose not to use \tilde{f} to calculate the internal energy or temperature.

Now let us introduce a new variable, the internal energy density distribution function:

$$g = \frac{(\boldsymbol{\xi} - \mathbf{u})^2}{2} f. \quad (10)$$

Notice that we define g using the real density distribution function f instead of \tilde{f} in the above equation. We call g the internal energy density distribution function because the

integral of g over the velocity space gives the internal energy density $\rho\epsilon$. ($\epsilon = DRT/2$ is the internal energy.) From the Boltzmann equation, Eq.(1), the evolution equation of this internal energy density distribution function is

$$\partial_t g + (\boldsymbol{\xi} \cdot \nabla)g = \frac{(\boldsymbol{\xi} - \mathbf{u})^2}{2}\Omega(f) - fq, \quad (11)$$

where the right-hand side of Eq.(11) is the heat dissipation term and

$$q = (\boldsymbol{\xi} - \mathbf{u}) \cdot [\partial_t \mathbf{u} + (\boldsymbol{\xi} \cdot \nabla)\mathbf{u}]. \quad (12)$$

Here we introduce a new collision model

$$\frac{(\boldsymbol{\xi} - \mathbf{u})^2}{2}\Omega(f) = -\frac{g - g^{eq}}{\tau_c}, \quad (13)$$

where

$$g^{eq} = \frac{\rho(\boldsymbol{\xi} - \mathbf{u})^2}{2(2\pi RT)^{D/2}} \exp\left[-\frac{(\boldsymbol{\xi} - \mathbf{u})^2}{2RT}\right]. \quad (14)$$

We will further assume that f in the last term of Eq.(11) can be replaced by \tilde{f} . As we will show next, these assumptions yield the correct macroscopic energy equation. Because Eq.(11) originates from the Boltzmann equation and describes the evolution of the internal energy distribution, we will call it the Boltzmann energy equation.

In summary, we propose to use the following equations to study thermal hydraulic problem:

$$\begin{aligned} \partial_t \tilde{f} + (\boldsymbol{\xi} \cdot \nabla)\tilde{f} &= -\frac{\tilde{f} - f^{eq}}{\tau_v}, \\ \partial_t g + (\boldsymbol{\xi} \cdot \nabla)g &= -\frac{g - g^{eq}}{\tau_c} - \tilde{f}(\boldsymbol{\xi} - \mathbf{u}) \cdot [\partial_t \mathbf{u} + (\boldsymbol{\xi} \cdot \nabla)\mathbf{u}], \end{aligned}$$

here

$$\begin{aligned} f^{eq} &= \frac{\rho}{(2\pi RT)^{D/2}} \exp\left[-\frac{(\boldsymbol{\xi} - \mathbf{u})^2}{2RT}\right], \\ g^{eq} &= \frac{\rho(\boldsymbol{\xi} - \mathbf{u})^2}{2(2\pi RT)^{D/2}} \exp\left[-\frac{(\boldsymbol{\xi} - \mathbf{u})^2}{2RT}\right]. \end{aligned}$$

The macroscopic variables are calculated using

$$\begin{aligned} \rho &= \int f d\boldsymbol{\xi}, \\ \rho\mathbf{u} &= \int \boldsymbol{\xi} f d\boldsymbol{\xi}, \\ \frac{\rho DRT}{2} &= \int g d\boldsymbol{\xi}. \end{aligned}$$

To better understand the Boltzmann energy equation, it is useful to examine the behavior of this equation in the long-wavelength and low-frequency limit. Following the Chapman–Enskog multiscale expansions, we expand the time derivative as $\partial_t = K \partial_{t_0} + K^2 \partial_{t_1} + \dots$, the space derivative as $\nabla = K \nabla_1$, and the density distribution function as $\tilde{f} = f^{eq} + K f^{(1)} + K^2 f^{(2)} + \dots$. The internal energy distribution function is similarly expanded as

$$g = g^{eq} + K g^{(1)} + K^2 g^{(2)} + \dots \quad (15)$$

Here the Knudsen number, K (the mean free path divided by the hydrodynamic length scale), is assumed to be a small parameter. Notice that both τ_c and q are first order in K . The reason $q \sim K$ is that q is proportional to \mathbf{u} .

To distinguish the different thermodynamic processes, we further split q in Eq.(12) into the following two terms:

$$q^I = \frac{1}{\rho} (\boldsymbol{\xi} - \mathbf{u}) \cdot (-\nabla p + \nabla \cdot \boldsymbol{\Pi}), \quad (16)$$

$$q^{II} = (\boldsymbol{\xi} - \mathbf{u})(\boldsymbol{\xi} - \mathbf{u}) : \nabla \mathbf{u}. \quad (17)$$

The first-order Chapman–Enskog approximation of Eq.(11) is

$$\partial_{t_0} g^{eq} + (\boldsymbol{\xi} \cdot \nabla_1) g^{eq} = -\frac{g^{(1)}}{\tau_c} - f^{eq} q. \quad (18)$$

The integral of the above equation over velocity space leads to

$$\partial_{t_0}(\rho \epsilon) + \nabla_1 \cdot (\rho \mathbf{u} \epsilon) = -p \nabla_1 \cdot \mathbf{u}, \quad (19)$$

which is exactly the macroscopic energy equation for Euler fluids. Notice that only q^{II} contributes to the compression work done by the pressure on the right-hand side.

The second-order Chapman–Enskog approximation of Eq.(11) is

$$\partial_{t_1} g^{eq} + [\partial_{t_0} + (\boldsymbol{\xi} \cdot \nabla_1)] g^{(1)} = -\frac{g^{(2)}}{\tau_c} - f^{(1)} q, \quad (20)$$

where

$$f^{(1)} = -\tau_v [\partial_{t_0} f^{eq} + \nabla_1 \cdot (\boldsymbol{\xi} f^{eq})] \quad (21)$$

is the standard first-order nonequilibrium deviation of the density distribution [3]. Substituting $f^{(1)}$ from Eq.(21) and $g^{(1)}$ from Eq.(18) into Eq.(20) and integrating Eq.(20) over velocity space, we have

$$\partial_{t_1}(\rho \epsilon) = \nabla_1 \cdot (\rho \chi \nabla \epsilon) + \boldsymbol{\Pi} : \nabla \mathbf{u}, \quad (22)$$

where the first term on the right-hand side represents heat conduction and the second term represents viscous heat dissipation. The coefficient $\chi = (D + 2)\tau_c RT/D$ is the thermal conductivity. It should be pointed out that q^I only affects the heat conduction term, while q^{II} only has an influence on the viscous dissipation term.

At this point, it is important to summarize the origins of three thermodynamic processes. First, the heat conduction term exclusively results from the second term on the left-hand side of Eq.(20), which only depends on the nonequilibrium term of the *internal energy density* distribution. Second, the viscous heat dissipation term results exclusively from the second term on the right-hand side of Eq.(20), which only depends on the nonequilibrium part of the *density* distribution. Third, the compression work done by the pressure in Eq.(19) is independent of both nonequilibrium distributions.

Finally, combining Eqs.(19) and (22), we can prove that Eq.(11) recovers the energy equation at the Navier–Stokes level:

$$\partial_t(\rho\epsilon) + \partial(\rho\mathbf{u}\epsilon) = \nabla \cdot (\rho\chi \nabla \epsilon) + \Pi : \nabla \mathbf{u} - p \nabla \cdot \mathbf{u}. \quad (23)$$

III. LATTICE BOLTZMANN THERMAL MODEL

In the previous section, we derived the continuous evolution equation for the internal energy density distribution—the Boltzmann energy equation. Our ultimate goal, however, is to develop a numerical algorithm which can be implemented on digital computers, because the analytical solution of Eqs.(1) and (11) is extremely difficult if not impossible. Our strategy is to derive two discrete evolution equations: one equation for the density distribution which governs the evolution of the density and velocity fields, and the other equation for the internal energy distribution which governs the evolution of the temperature field. Since the real density distribution f will not be mentioned again, we will omit the tilde of \tilde{f} in the following text.

A. The Lattice Boltzmann Equation for Density and Velocity Fields

It has been shown recently [20] that the lattice Boltzmann equation describing mass and momentum conservation can be derived from the Boltzmann equation. In this paper, we will extend that model to include an external force term, F ,

$$\frac{Df}{Dt} \equiv \partial_t f + (\boldsymbol{\xi} \cdot \nabla) f = -\frac{f - f^{eq}}{\tau_v} + F, \quad (24)$$

where

$$F = \frac{\mathbf{G} \cdot (\boldsymbol{\xi} - \mathbf{u})}{RT} f^{eq}, \quad (25)$$

with \mathbf{G} being the external force acting per unit mass [9]. Notice that $\int F d\boldsymbol{\xi} = 0$ and $\int F \boldsymbol{\xi} d\boldsymbol{\xi} = \rho \mathbf{G}$.

In most of the previous LBE models, the collision operator in the Boltzmann–BGK equation, Eq.(24), was assumed constant during each time step. This assumption introduces a second-order truncation error in the lattice Boltzmann equation [24]. For the LBE isothermal model, this truncation error was fortunately nondestructive because it can be totally absorbed into the physical viscous term. The only effect is a change of the viscosity from $\tau_v RT$ to $(\tau_v - 0.5\delta_t) RT$. (See [24] for more detailed discussions.)

For the thermal model, however, this second-order truncation error is no longer trivial. Here, the viscosity is involved not only in the momentum equation but also in the energy equation. To be specific, as shown in the previous section, the viscous heat dissipation

term in the energy equation exclusively comes from the nonequilibrium part of the density distribution. This term only depends on the first-order Chapman–Enskog approximation of the Boltzmann equation and is not affected by the second-order truncation error (which only appears in the second-order Chapman–Enskog expansion). In other words, the viscosity in the viscous heat dissipation term is always $\tau_v RT$, which is inconsistent with the viscosity in the LBE isothermal model mentioned above.

To eliminate this inconsistency, we adopt a second-order strategy to integrate the Boltzmann equation (24):

$$\begin{aligned} f(\mathbf{x} + \boldsymbol{\xi}\delta_t, \boldsymbol{\xi}, t + \delta_t) - f(\mathbf{x}, \boldsymbol{\xi}, t) = & -\frac{\delta_t}{2\tau_v} [f(\mathbf{x} + \boldsymbol{\xi}\delta_t, \boldsymbol{\xi}, t + \delta_t) - f^{eq}(\mathbf{x} + \boldsymbol{\xi}\delta_t, \boldsymbol{\xi}, t + \delta_t)] \\ & - \frac{\delta_t}{2\tau_v} [f(\mathbf{x}, \boldsymbol{\xi}, t) - f^{eq}(\mathbf{x}, \boldsymbol{\xi}, t)] \\ & + \frac{\delta_t}{2} F(\mathbf{x} + \boldsymbol{\xi}\delta_t, \boldsymbol{\xi}, t + \delta_t) + \frac{\delta_t}{2} F(\mathbf{x}, \boldsymbol{\xi}, t). \end{aligned} \quad (26)$$

The left-hand side results from the integral of the time derivative, $\partial_t + (\boldsymbol{\xi} \cdot \nabla)$, in Eq.(24). To avoid implicitness of this scheme, we further introduce a new variable:

$$\bar{f} = f + \frac{\delta_t}{2\tau_v} (f - f^{eq}) - \frac{\delta_t}{2} F. \quad (27)$$

The evolution equation for \bar{f} is

$$\bar{f}(\mathbf{x} + \boldsymbol{\xi}\delta_t, \boldsymbol{\xi}, t + \delta_t) - \bar{f}(\mathbf{x}, \boldsymbol{\xi}, t) = -\frac{\delta_t}{\tau_v + 0.5\delta_t} [\bar{f}(\mathbf{x}, \boldsymbol{\xi}, t) - f^{eq}(\mathbf{x}, \boldsymbol{\xi}, t)] + \frac{\tau_v F \delta_t}{\tau_v + 0.5\delta_t}. \quad (28)$$

To obtain the lattice Boltzmann model, the velocity space must be discretized as well. As shown in [20], to recover the continuity and momentum equations at the Navier–Stokes level, the microscopic velocity space must be discretized to guarantee that the zeroth through third moments of the equilibrium density distribution are exact. Note that the exactness of the fourth moment is not required here because the density distribution is only used to simulate the density and velocity fields. Expanding the Maxwell–Boltzmann equilibrium distribution, Eq.(6), up to \mathbf{u}^2 , the above criteria require the integral formula

$$\int \boldsymbol{\zeta}^m \exp(-\boldsymbol{\zeta}^2) d\boldsymbol{\zeta} = \sum_{\alpha} w_{\alpha} \boldsymbol{\zeta}_{\alpha}^m \quad (29)$$

to be exact from zeroth to fifth order ($m = 0, 1, \dots, 5$). For the two-dimensional case, applying the third-order Gauss–Hermite quadrature leads to the nine-speed LBE model with the discrete velocities

$$\mathbf{e}_{\alpha} = \begin{cases} \mathbf{0} & \alpha = 0, \\ (\cos[(\alpha - 1)\pi/2], \sin[(\alpha - 1)\pi/2])c & \alpha = 1, 2, 3, 4, \\ \sqrt{2}(\cos[(\alpha - 5)\pi/2 + \pi/4], \sin[(\alpha - 5)\pi/2 + \pi/4])c & \alpha = 5, 6, 7, 8, \end{cases} \quad (30)$$

where $c = \sqrt{3RT}$.

The macroscopic density and velocity can now be calculated using

$$\rho = \sum_{\alpha} \bar{f}_{\alpha}, \quad (31)$$

$$\rho \mathbf{u} = \sum_{\alpha} \mathbf{e}_{\alpha} \bar{f}_{\alpha} + \frac{\rho \mathbf{G} \delta_t}{2}. \quad (32)$$

The discrete density distribution, \bar{f}_{α} , satisfies the evolution equation

$$\bar{f}_{\alpha}(\mathbf{x} + \mathbf{e}_{\alpha} \delta_t, t + \delta_t) - \bar{f}_{\alpha}(\mathbf{x}, t) = -\frac{\delta_t}{\tau_v + 0.5\delta_t} [\bar{f}_{\alpha}(\mathbf{x}, t) - f_{\alpha}^{eq}(\mathbf{x}, t)] + \frac{\tau_v F_{\alpha} \delta_t}{\tau_v + 0.5\delta_t}, \quad (33)$$

where

$$F_{\alpha} = \frac{\mathbf{G} \cdot (\mathbf{e}_{\alpha} - \mathbf{u})}{RT} f_{\alpha}^{eq}. \quad (34)$$

The equilibrium distribution f_{α}^{eq} is given by

$$f_{\alpha}^{eq} = w_{\alpha} \rho \left[1 + \frac{3\mathbf{e}_{\alpha} \cdot \mathbf{u}}{c^2} + \frac{9(\mathbf{e}_{\alpha} \cdot \mathbf{u})^2}{2c^4} - \frac{3\mathbf{u}^2}{2c^2} \right], \quad (35)$$

where $w_0 = 4/9$, $w_{\alpha} = 1/9$ for $\alpha = 1, 2, 3, 4$, and $w_{\alpha} = 1/36$ for $\alpha = 5, 6, 7, 8$. Notice that the third moment of f_{α}^{eq} differs from its continuous counterpart, $\int \xi^3 f d\xi$, by a term with an order of \mathbf{u}^3 . In the incompressible limit, this difference can be neglected.

B. The Lattice Boltzmann Equation for the Temperature Field

As shown in the previous section, if the Boltzmann equation can be properly discretized in the temporal and velocity spaces so that the resulting discrete equation satisfies the mass and momentum conservation at the Navier–Stokes level, the final discrete scheme is exactly the lattice Boltzmann equation for isothermal flow. The same procedure can be applied to the Boltzmann energy equation. The resulting discrete scheme will serve as the lattice Boltzmann thermal equation which describes the evolution of the macroscopic temperature field.

Using the second-order temporal integration scheme, we integrate the Boltzmann energy equation, Eq.(11), in one time step:

$$\begin{aligned} & g(\mathbf{x} + \xi \delta_t, \xi, t + \delta_t) - g(\mathbf{x}, \xi, t) \\ &= -\frac{\delta_t}{2\tau_c} [g(\mathbf{x} + \xi \delta_t, \xi, t + \delta_t) - g^{eq}(\mathbf{x} + \xi \delta_t, \xi, t + \delta_t)] \\ &\quad - \frac{\delta_t}{2} f(\mathbf{x} + \xi \delta_t, \xi, t) q(\mathbf{x} + \xi \delta_t, \xi, t) - \frac{\delta_t}{2\tau_c} [g(\mathbf{x}, \xi, t) - g^{eq}(\mathbf{x}, \xi, t)] \\ &\quad - \frac{\delta_t}{2} f(\mathbf{x}, \xi, t) q(\mathbf{x}, \xi, t). \end{aligned} \quad (36)$$

Similarly, to avoid implicitness, we introduce a new variable:

$$\bar{g} = g + \frac{\delta_t}{2\tau_c} (g - g^{eq}) + \frac{\delta_t}{2} f q. \quad (37)$$

The evolution equation for \bar{g} is

$$\begin{aligned} & \bar{g}(\mathbf{x} + \boldsymbol{\xi}\delta_t, \boldsymbol{\xi}, t + \delta_t) - \bar{g}(\mathbf{x}, \boldsymbol{\xi}, t) \\ &= -\frac{\delta_t}{\tau_c + 0.5\delta_t} [\bar{g}(\mathbf{x}, \boldsymbol{\xi}, t) - g^{eq}(\mathbf{x}, \boldsymbol{\xi}, t)] - \frac{\tau_c}{\tau_c + 0.5\delta_t} f(\mathbf{x}, \boldsymbol{\xi}, t) q(\mathbf{x}, \boldsymbol{\xi}, t) \delta_t. \end{aligned} \quad (38)$$

Similarly, to derive a discrete scheme, the velocity space must be discretized appropriately. Needless to say, it will be most computationally efficient if we can use the same discretized velocities for both the mass density and energy density distributions in the LBE thermal model. To check whether this is possible, we first expand the equilibrium distribution of the internal energy density up to \mathbf{u}^2 :

$$\begin{aligned} g^{eq} &= \epsilon \frac{(\boldsymbol{\xi} - \mathbf{u})^2}{DRT} f^{eq} \\ &= \frac{\rho\epsilon}{(2\pi RT)^{D/2}} \exp\left(-\frac{\boldsymbol{\xi}^2}{2RT}\right) \left[\frac{\boldsymbol{\xi}^2}{DRT} + \left(\frac{\boldsymbol{\xi}^2}{DRT} - \frac{2}{D}\right) \frac{\boldsymbol{\xi} \cdot \mathbf{u}}{RT} \right. \\ &\quad \left. + \left(\frac{\boldsymbol{\xi}^2}{DRT} - \frac{4}{D}\right) \frac{(\boldsymbol{\xi} \cdot \mathbf{u})^2}{2(RT)^2} - \left(\frac{\boldsymbol{\xi}^2}{DRT} - \frac{2}{D}\right) \frac{\mathbf{u}^2}{2RT} \right]. \end{aligned} \quad (39)$$

As shown in Section II, the recovery of the macroscopic energy equation involves the zeroth through second moments of the equilibrium distribution of the internal energy density. Since the highest order of $\boldsymbol{\xi}$ in Eq.(39) is fourth, the quadrature, Eq.(29), for the thermal model will need to be accurate to sixth order. This implies that the third-order Gauss–Hermite quadrature chosen in the previous section is no longer valid.

At first glance, it seems that a higher-order quadrature is necessary for the thermal lattice Boltzmann equation. This apparent problem, however, can be avoided by regrouping Eq.(39):

$$\begin{aligned} g^{eq} &= \frac{\rho\epsilon}{(2\pi RT)^{D/2}} \exp\left(-\frac{\boldsymbol{\xi}^2}{2RT}\right) \left[\frac{\boldsymbol{\xi}^2}{DRT} + \left(\frac{\boldsymbol{\xi}^2}{DRT} - \frac{2}{D}\right) \frac{\boldsymbol{\xi} \cdot \mathbf{u}}{RT} + \frac{(\boldsymbol{\xi} \cdot \mathbf{u})^2}{2(RT)^2} - \frac{\mathbf{u}^2}{2RT} \right] \\ &\quad + \frac{\rho\epsilon}{(2\pi RT)^{D/2}} \exp\left(-\frac{\boldsymbol{\xi}^2}{2RT}\right) \left[\left(\frac{\boldsymbol{\xi}^2}{DRT} - \frac{D+4}{D}\right) \frac{(\boldsymbol{\xi} \cdot \mathbf{u})^2}{2(RT)^2} \right. \\ &\quad \left. - \left(\frac{\boldsymbol{\xi}^2}{DRT} - \frac{D+2}{D}\right) \frac{\mathbf{u}^2}{2RT} \right]. \end{aligned} \quad (40)$$

Through some straightforward algebra, it can be proved that the zeroth- through second-order moment of the second term of Eq.(40) vanishes. Consequently, this term can be eliminated from Eq.(40) without affecting the recovery of the macroscopic energy equation from the Boltzmann energy equation. The zeroth- through second-order moment of the remaining part of the energy equilibrium distribution involves only the zeroth- through fifth-order moment of Eq.(29). Therefore the third-order Gauss–Hermite quadrature is still valid. For the two-dimensional case, this leads to the nine-speed discrete velocity model, Eq.(30). With this velocity discretization, the internal energy density can now be calculated using

$$\rho\epsilon = \sum_{\alpha} \bar{g}_{\alpha} - \frac{\delta_t}{2} \sum_{\alpha} f_{\alpha} q_{\alpha}, \quad (41)$$

where

$$f_\alpha = \frac{\tau_v \bar{f}_\alpha + 0.5\delta_t f_\alpha^{eq} + 0.5\delta_t \tau_v F}{\tau_v + 0.5\delta_t}, \quad (42)$$

and

$$q_\alpha = (\mathbf{e}_\alpha - \mathbf{u}) \cdot \left[\frac{1}{\rho} (-\nabla p + \nabla \cdot \mathbf{\Pi}) + (\mathbf{e}_\alpha - \mathbf{u}) \cdot \nabla \mathbf{u} \right]. \quad (43)$$

The evolution equation for \bar{g}_α is

$$\begin{aligned} & \bar{g}_\alpha(\mathbf{x} + \mathbf{e}_\alpha \delta_t, t + \delta_t) - \bar{g}_\alpha(\mathbf{x}, t) \\ &= -\frac{\delta_t}{\tau_c + 0.5\delta_t} [\bar{g}_\alpha(\mathbf{x}, t) - g_\alpha^{eq}(\mathbf{x}, t)] - \frac{\tau_c}{\tau_c + 0.5\delta_t} f_\alpha(\mathbf{x}, t) q_\alpha(\mathbf{x}, t) \delta_t. \end{aligned} \quad (44)$$

By adopting the third-order Gauss–Hermite quadrature, the discrete internal energy density equilibrium distribution takes the form

$$\begin{aligned} g_0^{eq} &= -\frac{2\rho\epsilon}{3} \frac{\mathbf{u}^2}{c^2}, \\ g_{1,2,3,4}^{eq} &= \frac{\rho\epsilon}{9} \left[1.5 + 1.5 \frac{\mathbf{e}_\alpha \cdot \mathbf{u}}{c^2} + 4.5 \frac{(\mathbf{e}_\alpha \cdot \mathbf{u})^2}{c^4} - 1.5 \frac{\mathbf{u}^2}{c^2} \right], \\ g_{5,6,7,8}^{eq} &= \frac{\rho\epsilon}{36} \left[3 + 6 \frac{\mathbf{e}_\alpha \cdot \mathbf{u}}{c^2} + 4.5 \frac{(\mathbf{e}_\alpha \cdot \mathbf{u})^2}{c^4} - 1.5 \frac{\mathbf{u}^2}{c^2} \right]. \end{aligned} \quad (45)$$

Finally, the combination of Eqs.(41), (44), and (45) constitutes the lattice Boltzmann thermal equation.

C. Discretization of the Physical Space

In the previous two sections, we derived the lattice Boltzmann thermal model by discretizing the Boltzmann equation and the Boltzmann energy equation in temporal and velocity spaces. When implementing this model on digital computers, we must replace the continuous physical space by a series of grid nodes as well. Once the physical space is discretized, starting from the known information at the grid nodes, we can calculate thermohydrodynamical variables at the next time step using the evolution equations, Eqs.(33) and (44).

Notice that the calculated distributions at the next time step using this procedure may not reside on the grid nodes. A reconstruction step is necessary to compute the information on the grid nodes. Theoretically, there are many options for this reconstruction step. The easiest one is to discretize the physical space into a regular lattice so that every $\mathbf{x}_{node} + \mathbf{e}_\alpha \delta_t$ is another grid node. This way, the information at all the grid nodes is automatically known at the next time step. This has been the practice adopted in previous LBE isothermal models in which the lattice constant is chosen as $\delta_x = c\delta_t$. For simplicity, in this paper, we will continue to adopt this practice for our LBE thermal model. Furthermore, the characteristic speed c is taken to be a constant value, $c = \sqrt{3RT_0}$, where T_0 is the average temperature.

D. Boundary Conditions

The hydrodynamic boundary conditions for the lattice Boltzmann method have been studied extensively, and readers are referred to [1] for more details. In our study, we found

that the bounce-back rule of the nonequilibrium distribution proposed by Zou and He [26] is particularly useful and can be easily extended to impose thermodynamic boundary conditions. To understand the physical meaning of the bounce-back rule for the nonequilibrium distribution, we recall that in Grad's "13-moment" system [27], the nonequilibrium density distribution can be written as

$$f^{neq} = f^{eq} \left(\frac{\boldsymbol{\Pi} : (\boldsymbol{\xi} - \mathbf{u})(\boldsymbol{\xi} - \mathbf{u})}{2pRT} - \frac{\mathbf{S} \cdot (\boldsymbol{\xi} - \mathbf{u})}{2pRT} \left(1 - \frac{(\boldsymbol{\xi} - \mathbf{u})^2}{(D+2)RT} \right) \right), \quad (46)$$

where $\boldsymbol{\Pi}$ and \mathbf{S} are the stress tensor and heat flux vector, respectively. Because the nonequilibrium distribution itself is a small quantity, we can neglect all terms involving $O(\mathbf{u})$ and higher order. The leading term of the nonequilibrium discrete distribution becomes

$$f_{\alpha}^{neq} = w_{\alpha} \left(\frac{\boldsymbol{\Pi} : \mathbf{e}_{\alpha} \mathbf{e}_{\alpha}}{2(RT)^2} - \frac{\mathbf{S} \cdot \mathbf{e}_{\alpha}}{2(RT)^2} \left(1 - \frac{\mathbf{e}_{\alpha}^2}{(D+2)RT} \right) \right). \quad (47)$$

For isothermal problems, we neglect the heat transfer term, and the nonequilibrium density distribution can be approximated by

$$f_{\alpha}^{neq, iso} = \frac{w_{\alpha} \boldsymbol{\Pi} : \mathbf{e}_{\alpha} \mathbf{e}_{\alpha}}{2(RT)^2}. \quad (48)$$

Obviously, the following hydrodynamic boundary condition holds:

$$f_{\alpha}^{neq, iso} = f_{\beta}^{neq, iso}; \quad (49)$$

here \mathbf{e}_{α} and \mathbf{e}_{β} have opposite directions. This is exactly the bounce-back rule of the nonequilibrium density distribution proposed by Zou and He [26].

For thermal problems, neglecting again all terms involving $O(\mathbf{u})$, the nonequilibrium internal energy density distribution can be approximately written as

$$g_{\alpha}^{neq} = \mathbf{e}_{\alpha}^2 f_{\alpha}^{neq, iso} - w_{\alpha} \mathbf{e}_{\alpha}^2 \frac{\mathbf{S} \cdot \mathbf{e}_{\alpha}}{2(RT)^2} \left(1 - \frac{\mathbf{e}_{\alpha}^2}{(D+2)RT} \right). \quad (50)$$

This identity suggests the useful thermodynamic boundary condition

$$g_{\alpha}^{neq} - \mathbf{e}_{\alpha}^2 f_{\alpha}^{neq, iso} = - (g_{\beta}^{neq} - \mathbf{e}_{\beta}^2 f_{\beta}^{neq, iso}), \quad (51)$$

where \mathbf{e}_{α} and \mathbf{e}_{β} have opposite directions. Notice that, since the density distribution in our LBE thermal model does not take into account temperature variations, its nonequilibrium part satisfies the boundary condition, Eq.(49), and plays the role of $f^{neq, iso}$ in the boundary condition, Eq.(51).

IV. NUMERICAL SIMULATIONS

To test the new thermal lattice Boltzmann model, we have carried out numerical simulations for Couette flow with a temperature gradient and for Rayleigh-Bénard convection. For simplicity, we only carried out two-dimensional simulations although the extension to three dimensions is straightforward.

A. Couette Flow with a Temperature Gradient

Couette flow with a temperature gradient provides a good test of the ability of the new LBE thermal model to describe viscous heat dissipation. With the bottom wall fixed and the top boundary moving at the speed of U , the temperature profile must satisfy

$$\frac{T - T_0}{T_1 - T_0} = \frac{y}{H} + \frac{\text{PrEc}}{2} \frac{y}{H} \left(1 - \frac{y}{H}\right), \quad (52)$$

where T_0 and T_1 are the temperatures at the bottom and top boundaries, respectively; y is the distance from the bottom boundary; H is the height of the channel; $\text{Pr} = \nu/\chi$ is the Prandtl number; and $\text{Ec} = U^2/c_v(T_1 - T_0)$ is the Eckert number. No external force is involved in this problem.

To evaluate the accuracy of the new LBE thermal model, we carried out simulations for a wide range of both the Prandtl number and the Eckert number. Unless otherwise mentioned, we used throughout our simulations the following parameters: $U = 0.1c$, $H = 20$, $\tau_v = 0.5$, and $T_0 = 1$. All other parameters can be determined from the Prandtl and Eckert numbers. Periodic boundary conditions are used at the vertical boundaries, and the boundary conditions, Eqs.(49) and (51), are applied at the top and bottom walls.

Figure 1a shows the results for $\text{Pr} = 0.5$ and $\text{Ec} = 4, 20$, and 40 ; Fig. 1b shows the results for $\text{Ec} = 8$ and $\text{Pr} = 0.25, 1.25$, and 2.5 . Analytic solutions are also included for comparison. As shown, the numerical results agree with the analytic solutions. The numerical error is within the machine accuracy. The product PrEc represents the ratio between the viscous dissipation and the heat conduction. Our simulations span a wide range of values of PrEc . It is clear that our new LBE thermal model successfully simulates the viscous heat dissipation over this wide range.

Simulations were also carried out to study the τ_v , τ_c , and temperature ranges applicable for the new LBE thermal model. The scheme was found to be accurate and stable for both τ_v and τ_c ranging from 0.001 to 10, and for $(T_1 - T_0)/T_0$ ranging from 0 to 10. Compared with the multispeed LBE thermal models [13], the parameter ranges and the numerical stability are greatly increased.

B. Rayleigh–Bénard Convection

Another good benchmark test is Rayleigh–Bénard convection, in which a horizontal layer of viscous fluid is heated from the bottom while the top boundary is maintained at a lower temperature. A static solution exists for this problem, with the velocity zero everywhere and the temperature a linear function of the vertical coordinate. However, when the temperature between the top and bottom boundaries is increased above a certain threshold, the static conduction becomes unstable to any small disturbance and the system becomes convective.

Most of the previous studies on Rayleigh–Bénard convection were carried out in the framework of the Boussinesq approximation. With this approximation, all material properties are assumed to be constant except for the temperature dependence of the density in the gravity term. After absorbing the constant part of the gravity into the pressure, the effective external force can be written as [28]

$$\rho \mathbf{G} = \rho \beta g_0 (T - T_m) \mathbf{j}, \quad (53)$$

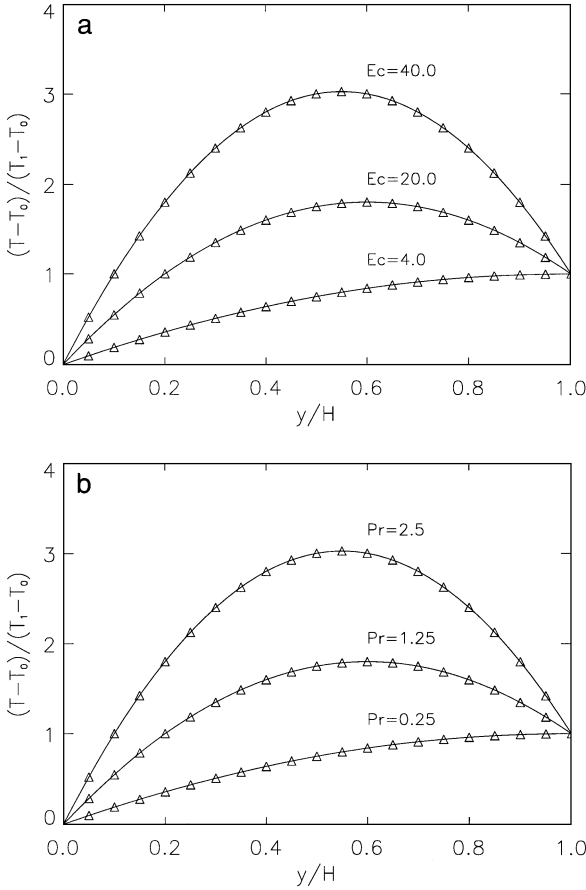


FIG. 1. Temperature profiles in Couette flow. The solid lines are the analytic results, while the symbols represent the LBE simulations. (a) $Pr = 0.5$, and (b) $Ec = 8$.

where β is the thermal expansion coefficient, g_0 is the acceleration due to gravity, T_m is the average value of the top and bottom temperatures, and the unit vector \mathbf{j} denotes the vertical direction opposite to that of gravity. The viscous heat dissipation is neglected.

To simulate Rayleigh–Bénard convection using the Boussinesq approximation, we have modified our LBE thermal model. First, we modified the model to be incompressible, and second, we deleted the viscous heat dissipation term. Details concerning these modifications can be found in the Appendix.

Linear stability theory has shown that the critical wave number for Rayleigh–Bénard convection is $k_c = 3.117$. This implies that the convection roll develops most readily in cells with an aspect ratio of $2\pi/k_c = 2.016$. Since our computational grid is a square lattice, we chose to use a channel with an aspect ratio of 2:1. The Prandtl number was fixed at 0.71. To ensure the code works in the near-incompressible regime, we fixed $\beta g_0 \Delta T H = 0.1$, where ΔT is the temperature difference between bottom and top walls, and H is the channel height. Unless otherwise mentioned, simulations were carried out on an 80×41 grid. Periodic boundary conditions are applied to the side boundaries. The boundary conditions, Eqs.(49) and (51), are applied at the top and bottom walls.

As the first test, we calculated the critical Rayleigh number, Ra_c , at which the static conductive state becomes unstable, where the Rayleigh number is defined as

$$Ra = \frac{\beta \Delta T g_0 H^3}{\nu \chi}. \quad (54)$$

The simulation began from a perturbed static conductive state. The initial temperature field was given by

$$T(x, y) = T_0 - \Delta T \frac{y}{H}, \quad (55)$$

and the initial pressure field was given by

$$p(x, y) = \left[1 + \frac{\rho \beta g_0 \Delta T y}{2} \left(1 - \frac{y}{H} \right) \right] \left[1 + 0.001 \cos \left(\frac{2\pi x}{L} \right) \right], \quad (56)$$

where L is the channel width.

At Rayleigh numbers below Ra_c , the perturbation dissipated and the maximum velocity in the flow region gradually decreased to zero, while at Rayleigh numbers above Ra_c , the maximum velocity eventually approached a finite value. The critical Rayleigh number was calculated by interpolating the growth rate of the maximum velocity at a slightly higher Rayleigh number and the decay rate at a slightly lower Rayleigh number. The calculated critical Rayleigh numbers are listed in Table I for various grids. The result is well converged and the final Ra_c agrees with the value of $Ra_c = 1707.76$ obtained by linear stability theory [29].

Once the Rayleigh–Bénard convection is established, the heat transfer between the top and bottom walls is greatly enhanced. The enhancement of the heat transfer can be described by the Nusselt number

$$Nu = 1 + \frac{\langle u_y T \rangle}{\chi \Delta T / H}, \quad (57)$$

where u_y is the vertical velocity, ΔT is the temperature difference between the bottom and top walls, H is the channel height, and $\langle \cdot \rangle$ represents the average over the whole flow domain. Figure 2 shows the calculated relationship between the Nusselt number and the Rayleigh number. Also included are the simulation results by Clever and Busse [30]. As shown, our results agree well with those by Clever and Busse for Rayleigh numbers less than 20,000. At higher Rayleigh numbers, the LBE simulation slightly underestimates the heat transfer. A similar trend was observed in the passive-scalar-based LBE study [18].

Typical temperature distributions and flow patterns of Rayleigh–Bénard convection at final steady states are plotted in Figs. 3 and 4 for $Ra = 5,000$, 10,000 and 50,000. As

TABLE I
Critical Rayleigh Number Obtained for Different
Grid Systems

Grid size	Ra_c	Error (%)
20×11	1759.36	3.02
40×21	1722.75	0.88
80×41	1713.48	0.33
160×81	1711.17	0.20
Theory	1707.76	—

Note. The error is calculated relative to the theoretical value.

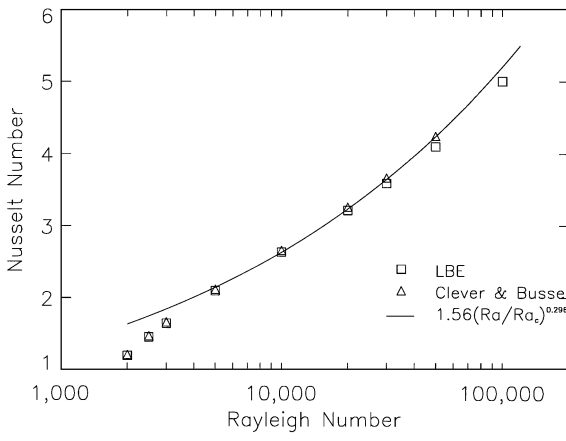


FIG. 2. The dependence of Nusselt number of Rayleigh number. Also included are simulation results by Clever and Busse [30], as well as the empirical formula $Nu = 1.56 (Ra/Ra_c)^{0.296}$.

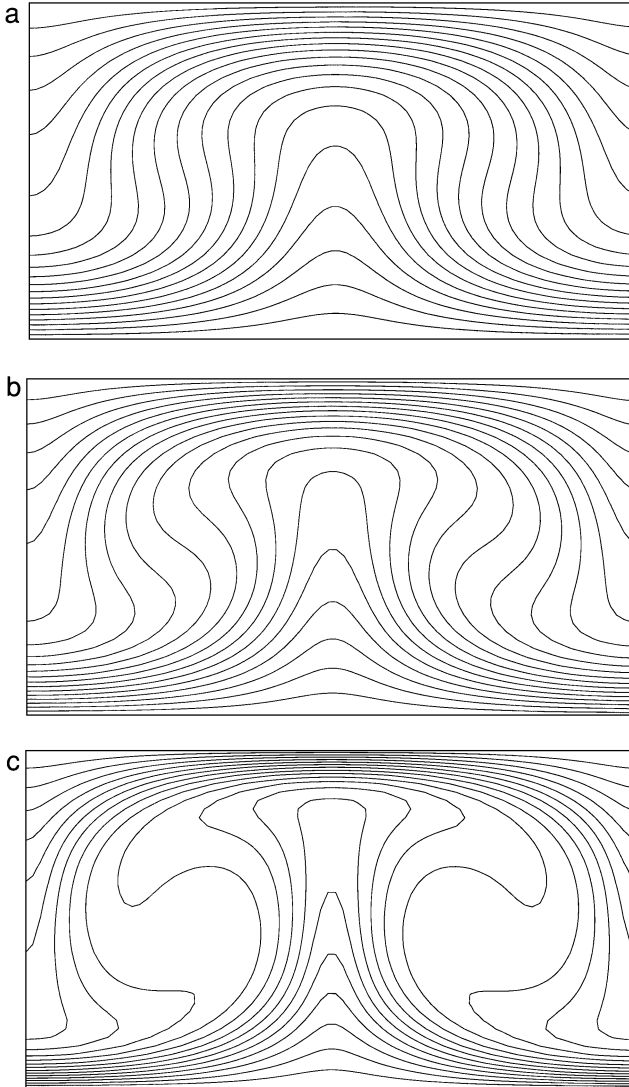


FIG. 3. The normalized temperature $(T - T_0)/\Delta T$ in Rayleigh-Bénard convection. (a) $Ra = 5,000$, (b) $Ra = 10,000$, and (c) $Ra = 50,000$. A total of 21 equally divided contours, with an interval of 0.05, are plotted.

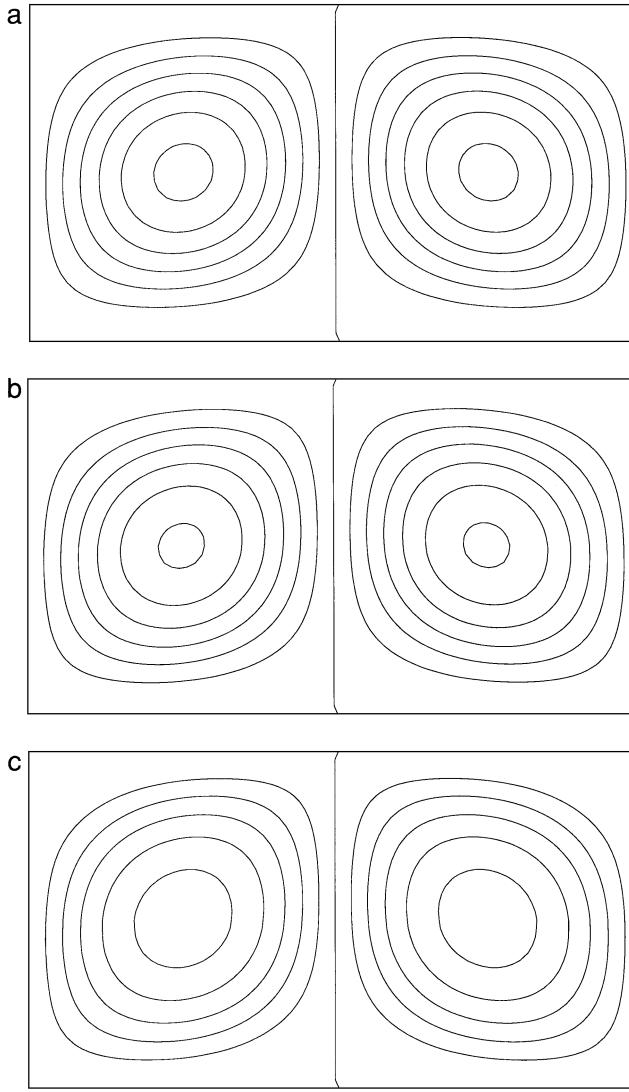


FIG. 4. Streamlines in Rayleigh–Bénard convection. (a) $Ra = 5,000$, (b) $Ra = 10,000$ and (c) $Ra = 50,000$. The stream function is in units of $v_{max} H$. The interval between contour lines is 0.05.

shown, hot fluids near the bottom wall flow upward and increase the temperature in the central portion of the channel, while cold fluids near the top wall flow downward and decrease the temperature near the side boundaries. When the Rayleigh number increases, two trends were observed for the temperature distribution: enhanced mixing of the hot and cold fluids, and an increase in the temperature gradients near the bottom and top boundaries. Both trends enhance the heat transfer in the channel.

Numerical instability has been a primary concern in previous multispeed LBE thermal models. In this study, it was found that the main parameters affecting the numerical stability are the relaxation times τ_v and τ_c . In the parameter range used in this study, the temperature variation appears to have a minor effect on numerical instability. The lowest value for either τ_v or τ_c was around 0.08 in simulation of Rayleigh–Bénard convection. This value seems to

be substantially higher than its counterpart in simulating the Couette flow with temperature gradient, but it is comparable to the lower limit found in simulations of complicated flows using LBE isothermal models [4,31]. In other words, our LBE thermal model has a numerical stability similar to previous LBE isothermal models. For this reason, we could simulate Rayleigh–Bénard convection at $Ra = 100,000$ on a 80×41 grid, while the highest Rayleigh number that the multispeed LBE thermal model could achieve on a 75×50 grid was around 8,000 [14].

V. CONCLUSION

A novel lattice Boltzmann thermal scheme has been developed to simulate thermohydrodynamics. Derived from the kinetic theory, this new scheme has a firm physical foundation. The key point in the new scheme is the use of two sets of distributions: the density distribution to simulate hydrodynamics and the internal energy distribution to simulate the thermodynamics. Compared with the passive-scalar-based LBE thermal models, the new scheme has the correct viscous heat dissipation and the correct compression work done by the pressure. Numerical experiments have shown that the new scheme has a better stability than multispeed LBE thermal models.

APPENDIX: LATTICE BOLTZMANN THERMAL MODEL FOR INCOMPRESSIBLE FLOW

In many applications, fluids are assumed to be incompressible and the viscous heat dissipation is intentionally neglected. It will be useful to modify our LBE thermal model to account for these variations. Following [32], we take into account the fact that the fluctuation of the density is small for incompressible fluids ($\sim M^2$ with M being the Mach number). By expanding the density around its average value, it can be proved that the density distribution for the incompressible LBE model is the same except that the equilibrium distribution becomes

$$f_{\alpha}^{eq} = w_{\alpha} \rho_0 \left[\frac{3p}{\rho_0 c^2} + \frac{3\mathbf{e}_{\alpha} \cdot \mathbf{u}}{c^2} + \frac{9(\mathbf{e}_{\alpha} \cdot \mathbf{u})^2}{2c^4} - \frac{3\mathbf{u}^2}{2c^2} \right], \quad (\text{A1})$$

where ρ_0 is the density which is constant. The pressure p replaces the density as the primary variable and it can be calculated as

$$p = \frac{c^2}{3} \sum f_{\alpha}^{eq}. \quad (\text{A2})$$

To delete the viscous heat dissipation and compression work done by the pressure, recall that both terms exclusively come from q^H in Eq.(12). Therefore, the LBE thermal model without the viscous heat dissipation and compression work done by the pressure is essentially the same as the one derived in Section III, except that the heat source term should only include q^I . Consequently, the heat source term in Eq.(43) is replaced by

$$q_{\alpha} = (\mathbf{e}_{\alpha} - \mathbf{u}) \cdot \left[\frac{1}{\rho_0} \nabla \cdot (-p\mathbf{I} + \mathbf{\Pi}) \right]. \quad (\text{A3})$$

REFERENCES

1. S. Chen and G. D. Doolen, Lattice Boltzmann method for fluid flows, *Ann. Rev. Fluid Mech.* **30**, 329 (1998).
2. D. O. Martínez, W. H. Matthaeus, S. Chen, and D. C. Montgomery, Comparison of spectral method and lattice Boltzmann simulations of two-dimensional hydrodynamics, *Phys. Fluids* **6**, 1285 (1994).
3. S. Hou, Q. Zou, S. Chen, G. D. Doolen, and A. Cogley, Simulation of cavity flow by the lattice Boltzmann method, *J. Comput. Phys.* **118**, 329 (1995).
4. X. He, L. S. Luo, and M. Dembo, Some progress in lattice Boltzmann method. I. nonuniform mesh grids, *J. Comput. Phys.* **129**, 357 (1996).
5. X. He and G. D. Doolen, Lattice Boltzmann method on curvilinear coordinates system: Flow around a circular cylinder, *J. Comput. Phys.* **134**, 306 (1997).
6. A. K. Gunstensen, D. H. Rothman, S. Zaleski, and G. Zanetti, Lattice Boltzmann model of immiscible fluids, *Phys. Rev. A* **43**, 4320 (1991).
7. X. Shan and H. Chen, Lattice Boltzmann model for simulating flows with multiple phases and components, *Phys. Rev. E* **47**, 1815 (1993).
8. M. R. Swift, W. R. Osborn, and J. M. Yeomans, Lattice Boltzmann simulation of nonideal fluids, *Phys. Rev. Lett.* **75**, 830 (1995).
9. X. He, X. Shan, and G. D. Doolen, A discrete Boltzmann equation model for non-ideal gases, *Phys. Rev. E* **57**, R13 (1998).
10. B. Ferreol, Lattice-Boltzmann simulations of flow through Fontainebleau sandstone, *Transport in Porous Media* **20**, 3 (1995).
11. G. McNamara and B. Alder, Analysis of the lattice Boltzmann treatment of hydrodynamics, *Physica A* **194**, 218 (1993).
12. F. J. Alexander, S. Chen, and J. D. Sterling, Lattice Boltzmann thermohydrodynamics, *Phys. Rev. E* **47**, R2249 (1993).
13. Y. Chen, H. Ohashi, and M. Akiyama, Thermal lattice Bhatnagar–Gross–Krook model without nonlinear deviations in macrodynamic equations, *Phys. Rev. E* **50**, 2776 (1994).
14. G. McNamara, A. L. Garcia, and B. J. Alder, Stabilization of thermal lattice Boltzmann models, *J. Statist. Phys.* **81**, 395 (1995).
15. P. Pavlo, G. Vahala, and L. Vahala, Higher order isotropic velocity grids in lattice methods, *Phys. Rev. Lett.* **80**, 3960 (1998).
16. P. Pavlo, G. Vahala, L. Vahala, and M. Soe, Linear-stability analysis of thermo-lattice Boltzmann models, *J. Comput. Phys.* **139**, 79 (1998).
17. A. Bartoloni, C. Battista, S. Cabasino, *et al.*, LBE simulation of Rayleigh–Bénard convection on the APE100 parallel processor, *Int. J. Mod. Phys. C* **4**, 993 (1993).
18. X. Shan, Solution of Rayleigh–Bénard convection using a lattice Boltzmann method, *Phys. Rev. E* **55**, 2780 (1997).
19. J. G. M. Eggels and J. A. Somers, Numerical simulation of free convective flow using the lattice Boltzmann scheme, *J. Heat Fluid Flow* **16**, 357 (1995).
20. X. He and L. Luo, A priori derivation of the lattice Boltzmann equation, *Phys. Rev. E* **55**, R6333 (1997).
21. T. Abe, Derivation of the lattice Boltzmann method by means of the discrete ordinate method for the Boltzmann equation, *J. Comput. Phys.* **131**, 241 (1997).
22. P. L. Bhatnagar, E. P. Gross, and M. Krook, A model for collision process in gases. I. Small amplitude processes in charged and neutral one-component system, *Phys. Rev.* **94**, 511 (1954).
23. C. Cercignani, The Boltzmann equation and its applications, in *Applied Mathematical Sciences* (Springer-Verlag, New York, 1988), Vol. 61.
24. J. D. Sterling and S. Chen, Stability analysis of lattice Boltzmann methods, *J. Comput. Phys.* **123**, 196 (1996).
25. N. Cao, S. Chen, S. Jin, and D. Martínez, Physical symmetry and lattice symmetry in the lattice Boltzmann method, *Phys. Rev. E* **55**, R21 (1997).

26. Q. Zou and X. He, On pressure and velocity boundary conditions for the lattice Boltzmann BGK model, *Phys. Fluids* **9**, 1591 (1997).
27. H. Grad, On the kinetic theory of rarefied gases, *Commun. Pure Appl. Math.* **2**, 331 (1949).
28. F. H. Busse, Transition to turbulence in Rayleigh–Bénard convection, in *Hydrodynamic Instability and the Transition to Turbulence*, edited by H. L. Swinney and J. P. Gollub (Springer-Verlag, Berlin, 1986).
29. W. H. Reid and D. L. Harris, Some further results on the Bénard Problem, *Phys. Fluids* **1**, 102 (1958).
30. R. M. Clever and F. H. Busse, Transition to time-dependent convection, *J. Fluid Mech.* **65**, 625 (1974).
31. X. He, L. Luo, and M. Dembo, Some progress in lattice Boltzmann method: Reynolds number enhancement in simulations, *Physica A* **239**, 276 (1997).
32. X. He and L. Luo, Lattice Boltzmann model for the incompressible Navier–Stokes equation, *J. Statist. Phys.* **88**, 927 (1997).